Response to Reviewers

Dear editor and reviewers:

Thank you very much for your letter and the constructive comments concerning our manuscript, now entitled "*Impacts of synoptic circulation types on nocturnal ozone increase in the North China Plain: Meteorological drivers and physical mechanisms*" (Manuscript ID: egusphere-2026-25).

We deeply appreciate the time and effort you have dedicated to reviewing our work. The insightful feedback has been exceedingly valuable in refining our terminology, strengthening our scientific arguments, and improving the overall quality of the paper. We have carefully considered all the comments and revised the manuscript accordingly.

General Update: Please note that to ensure absolute terminological rigor and to perfectly align with the reviewers' excellent suggestions, we have slightly adjusted the title from "...formation mechanisms" to "...physical mechanisms".

Please find below our detailed point-by-point responses to the specific comments as follows:

Reviewers' comments are in black.

Authors' responses are in blue.

Changes in the manuscript are in red.

Your Sincerely,

Liya Fan,

On behalf of the authors

Reviewer #2

General comments:

1. Scientific Significance of NOI: The introduction does not sufficiently justify the atmospheric importance of NOI episodes. A nighttime increase of 10 μg m^{-3} may be numerically detectable, but its impact on overall air quality or subsequent daytime peaks is not clearly established, particularly when background levels are low. The authors should better articulate the scientific or environmental relevance of studying these specific increments.

Response 1: Thanks for reviewer's comments. We have expanded the introduction to justify the scientific and environmental significance of NOI episodes beyond their numerical definitions. Specifically, we have emphasized two critical atmospheric impacts:

(1) Elevation of the next-day baseline:

Although the absolute nighttime O_3 concentration is generally lower than the daytime peak, NOI events induced by horizontal or vertical transport can markedly elevate the surface O_3 baseline on the following morning. A higher morning baseline concentration can lead to higher likelihood of O_3 exceedance.

(2) Altering nighttime atmospheric oxidative capacity (AOC):

Even under low background levels, sudden increments of nighttime O_3 actively drive nocturnal chemistry. Enhanced O_3 reacts with NO_2 to produce nitrate radicals (NO_3) and dinitrogen pentoxide (N_2O_5), which are vital precursors for secondary organic aerosols (SOA) and particulate nitrate. Thus, NOI is deeply coupled with nighttime $PM_{2.5}$ pollution.

We have integrated these mechanistic justifications into the third paragraph of the Introduction to explicitly establish the scientific relevance of studying these increments.

Lines 44-55:

Previously, nocturnal O_3 was often overlooked owing to its low concentrations. Although a quantitative threshold of a 10 μg m^{-3} hourly increase may appear modest during a clean night, the scientific and environmental significance of NOI episodes extends far beyond simple numerical detection. First, NOI events can occasionally result in a rapid surge in nighttime O_3 levels surpassing 160 μg m^{-3} (Wang et al., 2023b; Zhu et al., 2024), directly posing nocturnal threats to human health and plant stomatal uptake (Chowdhury et al., 2022; Hoshika et al., 2019). More

critically, even when absolute concentrations remain moderate, the horizontal or vertical transport of O_3-rich air that typically triggers NOI significantly elevates the surface O_3 baseline for the following morning. This higher initial baseline accelerates daytime accumulation, effectively exacerbating subsequent daytime photochemical smog (Wang et al., 2025). Furthermore, unexpected nighttime O_3 increments fundamentally alter the nocturnal atmospheric oxidative capacity (AOC). The enhanced O_3 facilitates dark reactions with nitrogen dioxide (NO_2) to generate nitrate radicals (NO_3) and dinitrogen pentoxide (N_2O_5), critical precursors for particulate nitrate and secondary organic aerosols (SOA), thereby linking NOI directly to regional fine particulate matter ($PM_{2.5}$) pollution (Wang et al., 2023a).

2. The NOI classification in Section 2.2 appears somewhat arbitrary. The unequal duration of the defined periods makes frequency comparisons statistically difficult. Furthermore, the transition from a time-based categorization to a weather-type categorization is abrupt and creates a disjointed narrative. The authors should harmonize these approaches or more clearly explain how the two frameworks intersect.

Response 2: Thanks for reviewer's comments. We have made the following revisions:

(1) Renaming the time-based categories:

We have abandoned the "Type A/B/C" nomenclature for occurrence times. They are now descriptively renamed as: Early-night NOI (EN): 20:00-23:00 LT (4 hour); Late-night NOI (LN): 00:00-06:00 LT (7 hour); Whole-night NOI (WN): Both EN and LN periods.

(2) Justification of unequal duration and arbitrary cutoffs:

The division between 23:00 and 00:00 is not mathematically arbitrary but physically rooted in the evolution of the nocturnal boundary layer. The EN period represents the transition phase where residual daytime turbulence may still exist. The LN period represents the deep-night phase where the surface inversion is fully established and highly stable. Even if we normalize the occurrences by the duration of the respective windows (yielding hourly occurrence rates), LN (9.93% per hour, 69.53% / 7 hour = 9.93%) still vastly outnumbers EN (5.42% per hour, 21.69% / 4 hour = 5.42%), proving that post-midnight events genuinely dominate.

(3) Harmonizing the narrative (bridging time and weather):

To eliminate the abrupt transition, we have added a bridging paragraph. We explicitly explain

that the time-based framework (identifying that most NOI occurs during the highly stable LN period) dictates the thermodynamic prerequisite. Breaking this late-night stability requires massive mechanical forcing, which directly motivates the second framework: the synoptic weather typing (identifying which specific weather systems provide this forcing).

We have revised Section 2.2 and the transition paragraphs in Section 3 to reflect these changes, thereby harmonizing the two approaches into a single, cohesive physical narrative.

Lines 132-137:

Rather than using arbitrary mathematical intervals, the specific timeframes for these types were chosen to perfectly align with the distinct physical evolution phases of the nocturnal boundary layer: (1) Early-night NOI (EN): The event occurs only between 20:00 and 23:00 LT, corresponding to the transitional boundary layer phase; (2) Late-night NOI (LN): The event occurs only between 00:00 and 06:00 LT, corresponding to the highly stable surface inversion phase; (3) Whole-night NOI (WN): The event occurs across both periods, persisting continuously through the night.

Lines 308-313:

As established in Section 3.1, the vast majority of NOI events in Xinxiang occur during the LN period. During this phase, the nocturnal boundary layer is characterized by a fully established surface inversion, creating a highly stable thermodynamic environment. To trigger downward O_3 transport under such extreme stability, localized residual turbulence is entirely insufficient. Instead, it requires massive, active mechanical forcing capable of physically breaking the inversion layer. Because such powerful mechanical triggers are fundamentally governed by macro-scale weather systems, identifying the specific synoptic circulations is the critical next step to unravel the forcing mechanisms behind these NOI events.

3. Station Typology: A critical omission is the lack of information regarding monitoring site classification (e.g., urban, rural, industrial). Since ozone concentrations are heavily influenced by local NO titration and precursor availability, the interpretation of NOI events is incomplete without considering the specific typology of the stations used in the study.

Response 3: Thanks for reviewer's comments. To clarify, the four stations (KF, DY, XY, and DX) selected for this study are all national air quality monitoring stations, specifically classified as urban

background/evaluation sites. They are primarily located within the urban area of Xinxiang, carefully sited to avoid direct micro-scale emission sources (e.g., immediate proximity to industrial facilities or major highway traffic).

Because these four stations share a highly consistent urban typology, they experience comparable regional chemical environments and baseline NO titration levels. This homogeneity in the local chemical sink is precisely what allows us to minimize localized chemical biases. Consequently, when concurrent NOI events are observed across these stations, we can confidently attribute them to overarching regional meteorological and dynamical drivers (as analyzed in Section 3), rather than localized chemical perturbations.

We have added this vital information regarding the monitoring site classification to Section 2.1 to provide a complete context for our interpretation of NOI events.

Lines 91-99:

It is important to note that all four stations are officially classified as urban evaluation sites located within the urban areas of Xinxiang. In this study, these four stations were deliberately selected due to their strong spatial representativeness over the urban core and their high data completeness. Because these stations share a consistent urban typology, they experience highly comparable baseline chemical environments (e.g., similar baseline nitrogen monoxide (NO) titration sinks and anthropogenic precursor availability). This spatial consistency is a crucial methodological design: it effectively minimizes random micro-scale chemical biases and isolated emission noise. By strictly controlling for these localized chemical heterogeneities, we ensure that the concurrent NOI events captured by this network genuinely reflect the overarching regional synoptic forcing and its subsequent, synchronized mechanical disruption of the local boundary layer, rather than random chemical artifacts.

4. Vertical Transport Analysis: The back-trajectory analysis is currently limited to the surface level. Given that the downward transport of ozone from the residual layer or upper troposphere is a well-documented driver of ozone increases, it is essential to include trajectories at higher altitudes to capture the full transport dynamics.

Response 4: Thanks for reviewer's comments. Initially, we considered running backward trajectories arriving at higher altitudes (e.g., 500m or 1000m). However, from a Lagrangian

transport perspective, an upper-level arriving trajectory only proves that air masses reached the upper boundary layer, but does not prove that those specific air masses subsequently intruded into the surface layer where the NOI was observed.

Therefore, to provide the most direct evidence of downward intrusion, we utilized a more robust approach: we extracted the 3D altitude-time cross-sections and pressure profiles of the trajectories arriving at the surface. This allows us to trace whether the surface-arriving air masses physically originated from the high-altitude residual layer over the preceding 48 hours.

As shown in the newly added 3D trajectory profiles (Figure S8 in the revised manuscript, corresponding to the right and left columns of the newly uploaded figure), the results provide spectacular Lagrangian evidence of massive subsidence:

(1) Under A-type, the primary clusters originated from ~800 hPa and ~900 hPa (approx. 1000-2000 m altitude) before continuously subsiding to the surface.

(2) Under C-type, an extremely prominent cluster rapidly subsided from the free troposphere (~700 hPa, >2000 m).

(3) Similar distinct subsiding pathways from the upper residual layer (~800-880 hPa) were observed under S-type and WNE-type.

This 3D Lagrangian evidence of synoptic-scale downward transport perfectly complements our local vertical mixing analysis (detailed in Section 3.4.2). Together, they form a complete 3D transport mechanism. We have completely revised Section 3.4.1 and added the 3D profile figures to incorporate this critical vertical dynamic analysis.

Lines 372-400:

3.4.1 3D regional transport and synoptic subsidence

To explore the triggering factors for the occurrence of NOI days under the four weather types, we investigated the 3D regional backward trajectories and CWT spatial distributions (Figs. 8, 9 and S8). While horizontal advection determines the regional source regions, the vertical profiles of these trajectories provide crucial Lagrangian evidence of downward transport.

Under A-type, air masses predominantly originated from the north (58.69%) (Fig. 8(a)). Crucially, the 3D altitude profiles (Fig. S8(a)-(b)) reveal that these dominant clusters originated from significantly high altitudes (~800 hPa) 48 hours prior, exhibiting continuous and massive subsidence as they approached Xinxiang. When these subsiding trajectories passed over the high O_3

potential source areas in northern Henan and western Shandong (CWT: 90-100 μg m^{-3}; Fig. 9(a)), regions well-documented for their heavy industrial facilities and intense precursor emissions (Lu et al., 2019; Li et al., 2019), they effectively entrained O_3-rich air from the residual layer downwards.

Under C-type, the airflow exhibited shorter trajectories and slower movement. Notably, the trajectory profile (Fig. S8(c)-(d)) captures an extremely dramatic vertical intrusion, where a specific cluster (21.43%) plunged directly from the lower free troposphere (~700 hPa, >2000 m) down to the surface. This intense vertical transport, coupled with high CWT values (~80 μg m^{-3}) over central/northern Henan (Fig. 9(b)), highlights the profound impact of deep vertical exchange driven by the cyclonic system.

Influenced by strong geostrophic winds under S-type, southwest airflow pathways dominated (Fig. 8(c)). The CWT analysis (Fig. 9(c)) identified a vast high-value source region (WCWT > 100 μg m^{-3}) encompassing the Central China urban agglomeration to the south, a vast region where intense anthropogenic NO_x and VOCs emissions continuously fuel massive daytime photochemical O_3 accumulation. The vertical profiles (Fig. S8(e)-(f)) confirm that a major portion of this southerly advection (~45.29%) subsided from the upper boundary layer (~880 hPa).

Finally, under WNE-type, the horizontal airflow was mainly concentrated on the northwest direction, accounting for 61.67% (Fig. 8(d)). The corresponding 3D altitude profiles (Fig. S8(g)-(h)) still capture a clear downward transport signal, revealing that this primary cluster originated from the upper residual layer (~800 hPa) 48 hours prior and subsided continuously. As these subsiding air masses passed over the potential source regions localized in central and northern Henan (CWT: 70-80 μg m^{-3}; Fig. 9(d)), they facilitated the downward entrainment and transport of O_3 to Xinxiang.

In summary, the 3D trajectory analysis demonstrates that the nocturnal O_3 spikes in Xinxiang are not merely driven by surface-level horizontal advection. Across all four weather types, the surface-arriving air masses systematically originated from the upper boundary layer or lower free troposphere, providing undeniable Lagrangian evidence of continuous downward O_3 transport from high-altitude reservoirs.

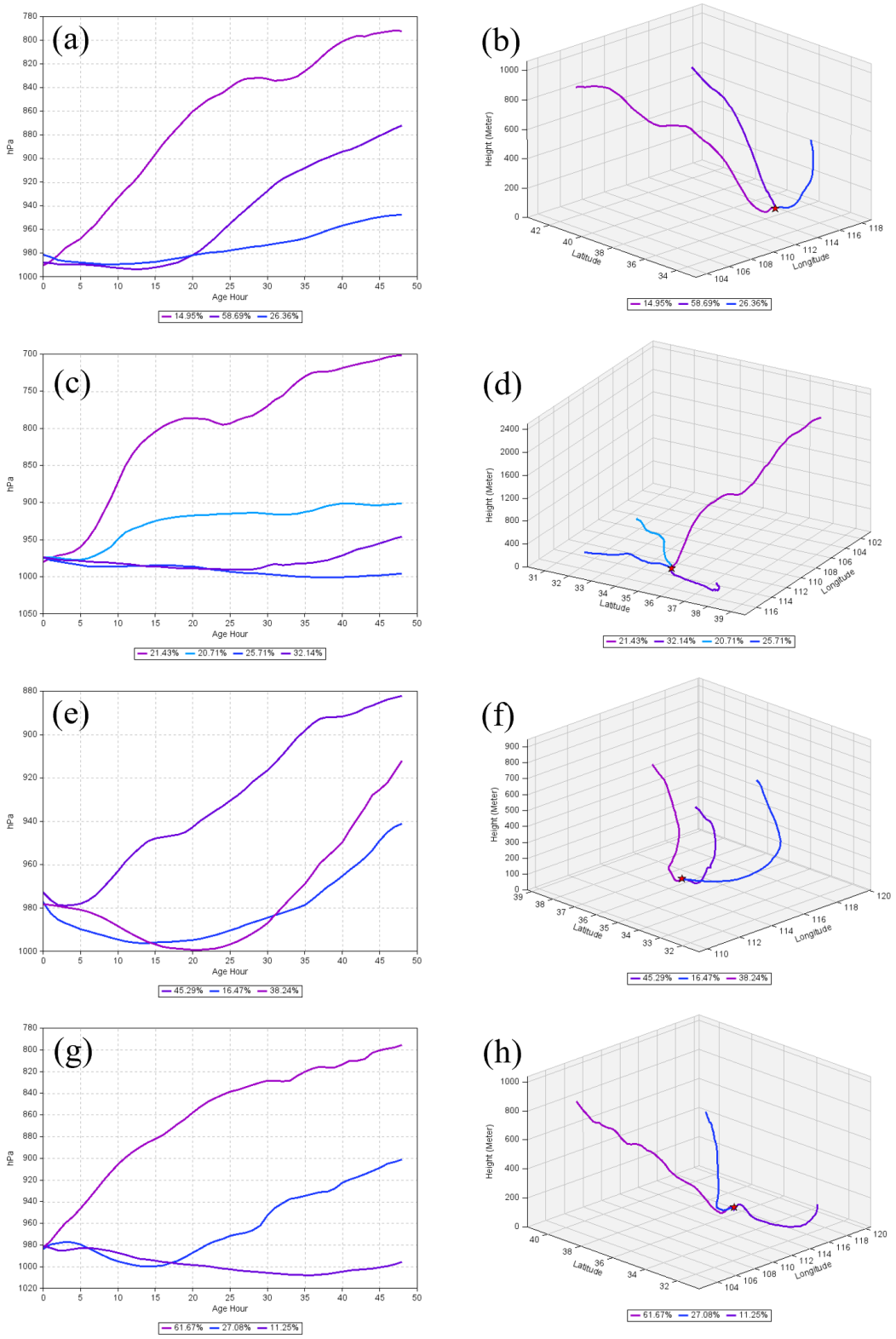

Figure S8: 3D clustered backward trajectories and their corresponding vertical pressure profiles for air masses arriving at Xinxiang under the four weather types. The left column (a), (c), (e), (g) displays the altitude-time cross-sections (represented by atmospheric pressure, hPa) of the trajectory clusters over the 48-hour backward tracking period. The right column (b), (d), (f), (h) illustrates the 3D spatial pathways of these clusters. The four

rows from top to bottom correspond to A-type (a, b), C-type (c, d), S-type (e, f), and WNE-type (g, h), respectively. The red star denotes the receptor site (Xinxiang). The percentages in the legends indicate the relative contribution of each trajectory cluster to the total trajectories under that specific weather type.

5. Causal Connections: While the manuscript provides a detailed description of meteorological features, it fails to sufficiently link these features to the underlying ozone phenomenology. The discussion often focuses on meteorological variables that may not be the primary drivers of ozone variability, leaving the physical connection between transport types and NOI poorly resolved.

Response 5: Thanks for reviewer's comments. The original manuscript, the discussion of meteorological features was overly descriptive and failed to explicitly establish the actual physical and dynamical pathways driving the nocturnal O_3 enhancements.

To address this critical flaw and establish the causal connections between weather types and the local O_3 phenomenology, we have completely restructured and rewritten Section 3.3. Instead of merely listing descriptive meteorological variables, the revised Section 3.3 now strictly constructs a causal chain for each weather type: macro-synoptic forcing, localized boundary-layer mechanical/thermodynamic perturbation and downward O_3 intrusion.

Specifically, we have explicitly resolved the physical causal connections through the following distinct pathways in the revised text:

(1) High-pressure subsidence (A-type): For calm conditions, we established a strict thermodynamic linkage. We explicitly linked the anticyclonic synoptic forcing to a highly stable, suppressed local environment with negative friction velocity anomalies (mean: $\Delta U^* = -0.01$ m s^{-1}). This severely suppresses general surface mechanical turbulence, serving as the essential thermodynamic and physical precondition that allows large-scale, high-pressure subsidence to dominate the column.

(2) Convective downdrafts and cold pools (C-type): Rather than simply mentioning general seasonal humidity, we causally linked the cyclonic low-pressure background and warm-wet moisture transport (mean: $\Delta RH = 4.08\%$) to amplified atmospheric thermodynamic instability.

(3) Intense mechanical shear and turbulent mixing (S-type & WNE-type): We shifted the focus from general wind speeds to specific mechanical turbulence metrics. As demonstrated in the revised

text, the intense synoptic pressure gradients directly cause massive localized spikes in friction velocity (mean: $\Delta U^* = 0.11$ m s^{-1} and 0.06 m s^{-1}) and massive boundary layer lifting (mean: $\Delta PBLH > 100$ m).

Instead of merely summarizing these changes, we want to transparently demonstrate how this causal logic has been explicitly woven into the narrative. Please find the fundamentally rewritten text of Section 3.3, which strictly follows this causal chain, provided below:

Lines 307-367:

3.3 Meteorological characteristics of primary weather types

As established in Section 3.1, the vast majority of NOI events in Xinxiang occur during the LN period. During this phase, the nocturnal boundary layer is characterized by a fully established surface inversion, creating a highly stable thermodynamic environment. To trigger downward O_3 transport under such extreme stability, localized residual turbulence is entirely insufficient. Instead, it requires massive, active mechanical forcing capable of physically breaking the inversion layer. Because such powerful mechanical triggers are fundamentally governed by macro-scale weather systems, identifying the specific synoptic circulations is the critical next step to unravel the forcing mechanisms behind these NOI events.

It should be noted that while seasonal variations significantly influence the daytime photochemical generation and absolute background concentrations of O_3, the nocturnal occurrence of NOI is predominantly driven by physical transport. As validated by the seasonal comparison (Fig. S6 and Text S3), while the absolute intensity of meteorological variables naturally fluctuates across seasons, the fundamental dynamical frameworks for a given weather type (e.g., the general orientation of horizontal pressure gradients and patterns of vertical motions) maintain functionally comparable mechanical triggers. Therefore, rather than focusing on seasonal background variations, our study focuses on elucidating these primary, synoptically-driven local meteorological drivers that trigger NOI.

The representative NOI days in Xinxiang were classified into four weather types (A-type, C-type, S-type, and WNE-type), with each exhibiting distinct meteorological features. Fig. 7 illustrates the spatial distributions of 850 hPa wind fields under four weather types. Under A-type, Xinxiang was located near a high-pressure center, with an outward-rotating wind field at 850 hPa (Figs. 5(a) and 7(a)), indicating the presence of an anticyclonic high-pressure system. Driven by this

synoptic forcing, Xinxiang experienced extremely calm conditions. As explicitly demonstrated by the nocturnal anomalies in Fig. 6 and Table S2, A-type was characterized by negative anomalies in wind speed (mean: ΔWS = -0.10 m s^{-1}) and friction velocity (mean: ΔU^* = -0.01 m s^{-1}), alongside a strongly constrained boundary layer (mean: $\Delta PBLH$ = 3.56 m, representing negligible expansion). This indicates that the overriding high-pressure system creates a highly stable environment. The explicit intrusion process of O_3 under this subsidence will be further verified in Section 3.4.

Under C-type, Xinxiang was dominated by low-pressure systems (Fig. 5(b)). At 850 hPa, a strong airflow originating near the coastal region of Guangxi Province moved continuously northeastward (Fig. 7(b)). This airflow not only moved at a high speed, but also likely carried substantial moisture, significantly enhancing atmospheric instability in its trajectory and surrounding regions (including Xinxiang), intensifying convective activity, and increasing the risk of heavy rainfall. Combined with the water vapor flux and divergence fields at 850 hPa, we find that the intense southwest warm-wet moisture transport belt under C-type is extremely prominent. Significant moisture convergence is observed along the entire path of this belt (including Xinxiang) (Fig. S7). Notably, the local meteorological anomalies perfectly capture this advection, with C-type uniquely coinciding with distinct positive anomalies in temperature (mean: ΔT = 2.60 °C) and the highest relative humidity anomaly among all weather types (mean: ΔRH = 4.08%). This localized warm and highly humid environment, dynamically coupled with a cyclonic low-pressure background, significantly amplifies atmospheric thermodynamic instability, highly favoring the development of regional convection and precipitation. Consequently, rather than uniform large-scale subsidence, NOI under C-type is primarily triggered by convective downdrafts and the subsequent development of cold pools.

S-type represents a dynamic environment driven by distinct horizontal advection. Under S-type, Xinxiang was situated in a tight pressure gradient, typically between a western low and an eastern high (Figs. 5(c) and 7(c)). Driven by this synoptic setup, continuous southerly geostrophic winds prevailed over the region. As detailed in Table S2, S-type produced significant positive anomalies in local wind speed (mean: ΔWS = 0.54 m s^{-1}) and friction velocity (mean: ΔU^* = 0.06 m s^{-1}). These specific values rigorously demonstrate that beyond facilitating regional horizontal transport (which will be explicitly traced in Section 3.4.1), the southerly advection directly generates substantial localized mechanical turbulence at the surface, physically lifting the nocturnal boundary layer

(mean: ΔPBLH = 102.41 m). This localized mechanical shear serves as the direct trigger for breaking nocturnal stability, subsequently entraining O_3-rich air from the elevated residual layer down to the surface and triggering NOI events.

Although Xinxiang often featured a massive continental high-pressure system (e.g., the Siberian High) to the northwest under WNE-type (Fig. 5(d)), their local dynamics are fundamentally different from the pure subsidence of A-type. At 850 hPa, the region was obviously influenced by a northwestern airflow (Fig. 7(d)), consistent with the geostrophic wind characteristics of WNE-type. Unlike A-type, where the study area sits calmly at the high-pressure center, under WNE-type, Xinxiang was located at the densely packed periphery of the advancing high. Consequently, the macroscopic forcing shifts to intense horizontal pressure gradients (Figs. 5(d) and 7(d)). This kinematic distinction is perfectly captured by the localized surface anomalies (Table S2). WNE-type exhibited the most extreme positive anomalies among all categories, with local wind speed (mean: ΔWS = 1.74 m s^{-1}) and friction velocity (mean: ΔU^* = 0.11 m s^{-1}) far exceeding other types. Driven by this intense horizontal advection and wind shear, the nocturnal boundary layer experienced massive mechanical lifting (mean: ΔPBLH = 156.22 m). Furthermore, this intense mechanical mixing effectively breaks the nocturnal surface inversion, bringing slightly warmer air from aloft downward (detailed mechanism analysis is presented in Section 3.4.2). This vigorous downward mixing of the elevated residual layer shares conceptual similarities with the nocturnal fumigation-like processes documented in other literature (Wu et al., 2023; He et al., 2022), which also explains the observed positive temperature anomaly (mean: ΔT = 0.77 °C). Therefore, despite the high-pressure background, it is this extraordinarily strong localized shear and turbulent mixing, that serves as the primary mechanical driver forcing O_3 downward to the surface during WNE-type. Combined with rapid dispersion of local NO emissions under high winds that greatly mitigates nighttime titration, vigorous vertical entrainment counteracts both horizontal diffusion and titration loss of O_3, and ultimately causes a net O_3 surge.

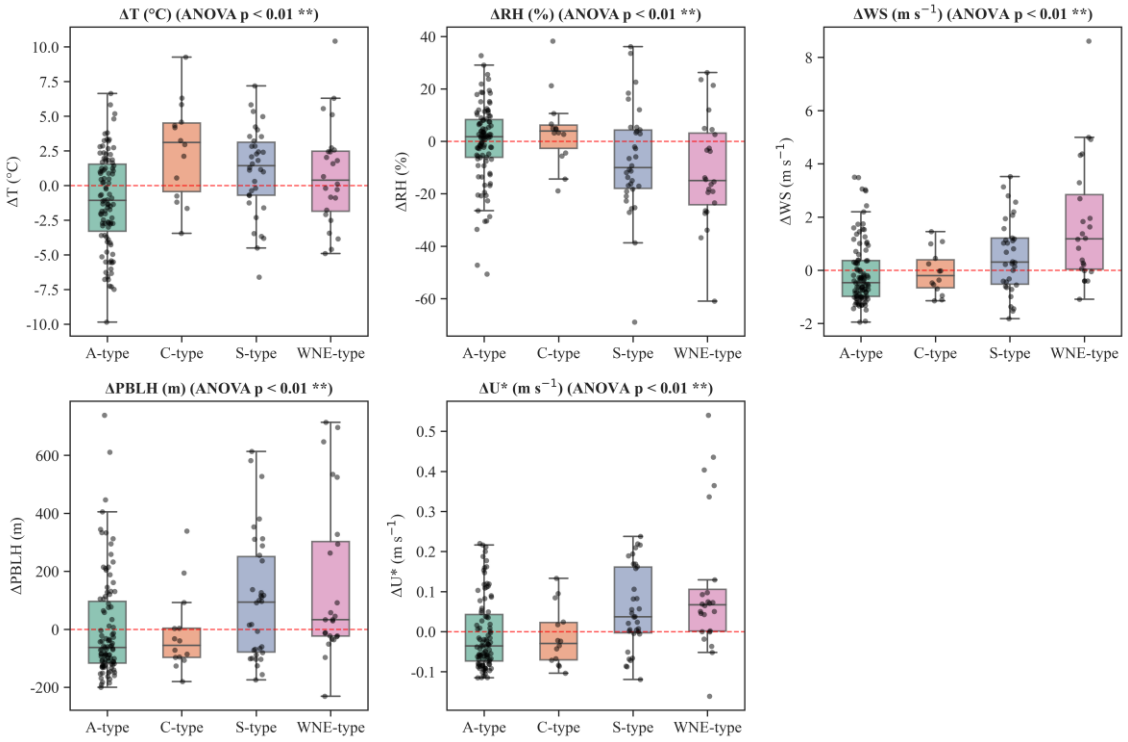

Figure 6: One-Way ANOVA results for key meteorological variables (T, RH, WS, PBLH and U^*) of different synoptic categories. In each boxplot, the central black solid line indicates the median. The horizontal red dashed line denotes the zero-anomaly reference.

Table S2. Statistical summary of nocturnal meteorological anomalies and ANOVA results under the four weather types.

Variable	A-type	C-type	S-type	WNE-type	p-value
ΔT (°C)	-1.07 ± 3.41	2.60 ± 3.54	1.06 ± 3.18	0.77 ± 3.70	$< 0.01^{**}$
ΔRH (%)	-0.31 ± 14.82	4.08 ± 14.00	-7.12 ± 20.46	-11.15 ± 20.72	$< 0.01^{**}$
ΔWS (m s^{-1})	-0.10 ± 1.21	-0.08 ± 0.83	0.54 ± 1.39	1.74 ± 2.32	$< 0.01^{**}$
ΔPBLH (m)	3.56 ± 178.15	-14.44 ± 139.19	102.41 ± 216.82	156.22 ± 274.82	$< 0.01^{**}$
ΔU^* (m s^{-1})	-0.01 ± 0.09	-0.01 ± 0.07	0.06 ± 0.10	0.11 ± 0.17	$< 0.01^{**}$

Note: Data are presented as Mean ± Standard Deviation. The anomalies (Δ) were calculated relative to their respective monthly nocturnal means. The p-values are derived from One-Way ANOVA tests indicating statistical significance under the four weather types.

6. The occurrence of NOI cannot be related solely with long-range transport ignoring local/regional features.

Response 6: Thanks for reviewer's comments. We have restructured the manuscript (specifically

Section 3.4.2) to explicitly couple overarching synoptic transport with critical local/regional features.

As detailed in the revised manuscript, we have now incorporated several key local features to explain the physical triggering of NOI:

(1) Subsidence-driven compression (A-type): This weather type is strictly dominated by systematic high-pressure subsidence. Wind shear breaks down the nocturnal inversion layer, increasing near-surface atmospheric instability and intensifying turbulent mixing, which transports O_3 from the residual layer down to the surface.

(2) Thermodynamically-driven convective mixing (C-type): Distinct from uniform subsidence, this mechanism is driven by localized mesoscale thermodynamics. Triggered by a cyclonic low-pressure background and intense moisture advection, the downward transport is dominated by the cold-pool downdrafts and shallow convection.

(3) Shear-driven mechanical entrainment (S-type and WNE-type): Both of these patterns are primarily controlled by synoptically-driven intense wind shear, utilizing massive horizontal advection to physically rupture the nocturnal inversion layer.

In our current narrative, regional transport (Section 3.4.1) is explicitly framed merely as the delivery mechanism that supplies the high-altitude O_3 reservoir, while the local and regional features (Section 3.4.2) are identified as the essential mechanical triggers that bring it down to the surface.

Lines 406-451:

3.4.2 Vertical mixing and mechanical triggers

As established in Section 3.4.1, 3D trajectories confirm the synoptic delivery of air masses from high altitudes. However, to translate these high-altitude arrivals into surface NOI events, specific vertical transport mechanisms are required. To validate this process, we analyzed the vertical profiles of pressure velocity (Fig. 10), thermodynamic stability (Fig. S9), O_3 concentrations (Fig. S10), and surface turbulence metrics (Fig. 11).

The vertical O_3 profiles (Fig. S10) first confirm the fundamental prerequisite for NOI across all weather types: following sunset, a distinct nocturnal residual layer (RL) forms, clearly indicated by the high O_3 concentrations. Shielded from surface NO titration and dry deposition, this RL successfully retains high daytime O_3, serving as the localized O_3 reservoir waiting to be tapped by

downward forcing.

For A-type, the intrusion is primarily initiated by the systematic macroscopic subsidence of the continental high-pressure system. As explicitly shown in Fig. 10(a), a robust macro-scale downdraft dominates the vertical column over the Xinxiang region. This subsidence induces profound adiabatic compression, forming a significant low-level temperature inversion (1000-950 hPa) accompanied by low mid-level RH (Fig. S9). The inversion layer acts as a dynamic barrier, leading to marked vertical gradients in horizontal wind and sinking velocity and generating localized vertical wind shear. While the overall nocturnal surface environment remains highly stable and suppressed (consistent with the negative mean ΔU^* anomaly in Table S2), this localized shear interaction triggers intermittent, transient bursts of mechanical turbulence. These brief turbulent eddies, evidenced by the distinct nocturnal fluctuations in U^* (Fig. 11), provide enough mechanical mixing to efficiently entrain the O_3-rich air from the residual layer down to the surface.

Under C-type, vertical mixing is dominated by localized mesoscale thermodynamics rather than uniform synoptic subsidence. As seen in Fig. 10(b), the vertical velocity field exhibits a complex coexistence of localized downdrafts and updrafts. The thermodynamic profiles (Fig. S9) corroborate this with a temperature inversion and mid-level dry air entrainment. This aligns perfectly with the cold pool mechanism: following convective rainfall, surface evaporative cooling generates a dense, subsiding pool of cold air. Simultaneously, the moderate CAPE values (86-314 J kg^{-1}) indicate residual thermodynamic instability driving localized shallow convection. The intense collision between these subsiding cold pools and localized convective motions creates severe turbulent mixing. This translates into the sharp nocturnal fluctuations in U^* (Fig. 11), thereby increasing instability and dragging O_3-rich air from the RL into the surface.

The local triggering mechanism under S-type relies fundamentally on intense mechanical shear overriding macro-scale lifting. S-type features strong southerly geostrophic winds. As this intense airflow approaches Xinxiang, it is forced upward by the Taihang Mountains, generating pronounced macro-scale orographic updrafts (Fig. 10(c)). However, to achieve the downward transport of O_3 against this macroscopic background lifting, a highly aggressive, localized boundary-layer mixing mechanism is essential. Specifically, the moderate CAPE values (257-295 J kg^{-1}) indicate persistent thermodynamic instability (Fig. S9), which fuels localized shallow convective motions within the nocturnal boundary layer. Simultaneously, anomalously strong near-surface horizontal winds (mean:

ΔWS = 0.54 m s^{-1}; Table S2) forcefully interact with surface friction, inducing severe mechanical wind shear. The powerful synergy of this thermal instability and mechanical shear explicitly manifests as massive, sharp nocturnal spikes in U^* and PBLH (Table S2 (mean: ΔPBLH = 102.41 m, ΔU^* = 0.06 m s^{-1}) and Fig. 11). Ultimately, this exceptionally enhanced turbulent mixing mechanically erodes the stable nocturnal inversion, overpowering the macroscopic updrafts to aggressively drag aloft O_3 from the residual layer down to the surface.

Finally, under WNE-type, downward transport is facilitated by an advection-driven mechanical shear mechanism. As explicitly shown in Fig. 10(d), the lower troposphere (below 850 hPa) is dominated by intense macro-scale subsidence. This induces a strong temperature inversion and extreme thermodynamic stability, corroborated by low CAPE values (22-23 J kg^{-1}) (Fig. S9), meaning thermal convective motions are completely suppressed. However, WNE-type is simultaneously driven by intense horizontal advection. As this robust horizontal airflow passes over Xinxiang, intense near-surface vertical wind shear is produced. This macroscopic advective forcing translates directly into massive nocturnal spikes in boundary-layer turbulence, explicitly captured by U^* and PBLH (Table S2 (mean: ΔPBLH = 156.22 m, ΔU^* = 0.11 m s^{-1}) and Fig. 11). This enhanced nocturnal turbulence drives the downward transport of O_3 from the residual layer to the surface, thereby triggering the NOI events.

Specific comments:

1. Line 48: Please expand on the specific negative impacts of NOI to underscore the environmental importance of the study.

Response 1: Thanks for reviewer's comments. We have expanded the relevant discussion in the Introduction. Rather than solely focusing on the direct health effects, we have now detailed three major environmental and atmospheric consequences of NOI:

(1) Direct toxicity: Rapid surges in nighttime O_3 (occasionally surpassing 160 μg m^{-3}) directly pose nocturnal threats to human health and exacerbate plant stomatal uptake.

(2) Exacerbation of daytime photochemical smog: We emphasized that horizontal or vertical transport of O_3-rich air elevates the surface O_3 baseline for the following morning, accelerating daytime accumulation and worsening subsequent photochemical smog.

(3) Alteration of atmospheric oxidative capacity (AOC): We linked NOI to the broader issue of regional fine particulate matter ($PM_{2.5}$) pollution, explaining how enhanced nocturnal O_3 facilitates dark reactions (generating NO_3 and N_2O_5), which are critical precursors for secondary organic aerosols (SOA) and particulate nitrates.

Lines 45-55:

Although a quantitative threshold of a 10 μg m^{-3} hourly increase may appear modest during a clean night, the scientific and environmental significance of NOI episodes extends far beyond simple numerical detection. First, NOI events can occasionally result in a rapid surge in nighttime O_3 levels surpassing 160 μg m^{-3} (Wang et al., 2023b; Zhu et al., 2024), directly posing nocturnal threats to human health and plant stomatal uptake (Chowdhury et al., 2022; Hoshika et al., 2019). More critically, even when absolute concentrations remain moderate, the horizontal or vertical transport of O_3-rich air that typically triggers NOI significantly elevates the surface O_3 baseline for the following morning. This higher initial baseline accelerates daytime accumulation, effectively exacerbating subsequent daytime photochemical smog (Wang et al., 2025). Furthermore, unexpected nighttime O_3 increments fundamentally alter the nocturnal atmospheric oxidative capacity (AOC). The enhanced O_3 facilitates dark reactions with nitrogen dioxide (NO_2) to generate nitrate radicals (NO_3) and dinitrogen pentoxide (N_2O_5), critical precursors for particulate nitrate and secondary organic aerosols (SOA), thereby linking NOI directly to regional fine particulate matter ($PM_{2.5}$) pollution (Wang et al., 2023a).

2. Line 64: Provide more comprehensive metadata for the study area, including population density in Xinxiang, primary precursor sources, and general climatological characteristics.

Response 2: Thanks for reviewer's comments. In the revised manuscript (Introduction), we have expanded the description of the study area to include the three specific aspects reviewer suggested:

(1) Population metadata: We added the demographic context, noting that Xinxiang is a densely populated urban center with a population exceeding 6 million and a density of over 700 persons km^{-2}.

(2) Climatological characteristics: We specified that the region experiences a typical temperate continental monsoon climate, characterized by hot, humid summers and cold, dry winters.

(3) Primary precursor sources: We clarified that the primary O_3 precursors (NO_x and VOCs)

predominantly originate from local heavy industrial facilities (e.g., chemical and manufacturing plants), intense vehicular exhaust from its transportation networks, and solvent usage.

By incorporating these detailed regional characteristics, the rationale for selecting Xinxiang as a critical representative case study in the North China Plain has been greatly strengthened.

Lines 73-80:

Located in the southern NCP, Xinxiang is bordered by the Taihang Mountains to the north and the Yellow River to the south (Fig. S1). As a densely populated urban center (with a population exceeding 6 million and a high population density of over 700 persons km^{-2}), Xinxiang features a typical temperate continental monsoon climate, characterized by hot, humid summers and cold, dry winters. Furthermore, serving as a major industrial and transportation hub in Henan Province, the city experiences intense anthropogenic emissions. The primary precursors for O_3 (i.e., NO_x and VOCs) predominantly originate from heavy industrial facilities (e.g., chemical and manufacturing plants), intense vehicular exhaust along major transportation arteries, and solvent usage. This unique topography, combined with these high baseline emissions and specific climatological conditions, makes Xinxiang a critical case study for understanding NOI.

3. Section 2.1: It is essential to specify the spatial and temporal resolutions of the MERRA-2 and ERA5 datasets used.

Response 3: Thanks for reviewer's comments. In the revised manuscript (Section 2.1), we have now added the spatial and temporal resolutions for both datasets:

Lines 99-103:

Sea level pressure (SLP) data and 17-layer vertical profiles (500-1000 hPa) of vorticity, wind speed (WS), wind direction, temperature (T), relative humidity (RH) and O_3 concentration were acquired from the Modern-Era Retrospective Analysis for Research and Applications dataset (MERRA-2, Version 2, with a spatial resolution of 0.5° × 0.625° and temporal resolutions of 1 hour for surface data and 3 hours for 3D vertical profiles) (https://disc.gsfc.nasa.gov/).

Lines 106-110:

Additionally, specific humidity (850hpa), planetary boundary layer height (PBLH), friction velocity (U^*), and convective available potential energy (CAPE) were derived from the ERA5

reanalysis dataset (https://www.ecmwf.int/en/forecasts/dataset/ecmwf-reanalysis-v5) (with a spatial resolution of 0.25° × 0.25° and an hourly temporal resolution) provided by the European Centre for Medium-Range Weather Forecasts (ECMWF), which offers superior boundary layer parameters (Hersbach et al., 2020; Bell et al., 2021).

4. Section 2.3: The use of Sea Level Pressure (SLP) for the Lamb-Jenkinson classification may overlook transport occurring at higher altitudes. I suggest incorporating data from higher geopotential heights to ensure the synoptic classification is representative of the layers where ozone transport is most active.

Response 4: Thanks for reviewer's comments. We have considered substituting the input data. However, we encountered a strict methodological limitation inherent to the Lamb-Jenkinson (L-J) objective weather typing method itself. We ultimately had to retain SLP as the primary input based on the following practical and physical considerations, but we took an alternative verification approach:

(1) The strict algorithmic constraint of the L-J method: The L-J classification algorithm is mathematically strictly defined and calibrated exclusively for Sea Level Pressure (SLP) fields. Its core mathematical framework and the specific threshold criteria used to assign the 27 weather types are rigidly normalized for surface-level pressure gradients. Attempting to substitute SLP with upper-level geopotential heights fundamentally breaks the method's original algorithmic constraints, making it impossible to derive valid classification indices.

(2) Cross-validating SLP types with high-altitude transport: To strictly adhere to the established L-J mathematical methodology while fully addressing reviewer's valid concern regarding high-altitude transport, we took an alternative verification approach. Because macro-scale synoptic systems are typically deep, equivalent-barotropic systems, we extracted the 850 hPa wind fields and overlaid them directly onto our SLP-derived weather types (Fig. S5).

As explicitly demonstrated in Fig. S5, the spatial patterns of the 850 hPa wind flow exhibit a near-perfect coupling with the SLP-defined synoptic types. This verification ensures that while our algorithm relies on SLP to satisfy its mathematical requirements, the resulting weather types successfully and comprehensively represent the very high-altitude transport circulations.

Lines 257-263:

Fig. S4 displays the mean SLP of representative NOI days under different weather types from 2021 to 2023. It can be seen that the position of high- and low-pressure centers exhibit certain discrepancies among different weather types. Furthermore, to explicitly validate that this SLP-based classification accurately captures airflow characteristics in lower troposphere, Fig. S5 illustrates the spatial distributions of mean SLP overlaid with 850 hPa wind fields for the 20 identified weather types. The spatial patterns demonstrate a high degree of physical consistency, wherein the surface pressure gradients align with the 850 hPa wind field. This confirms that the SLP-based Lamb-Jenkinson method is highly robust and effectively represents synoptic circulation background of upper boundary-layer.

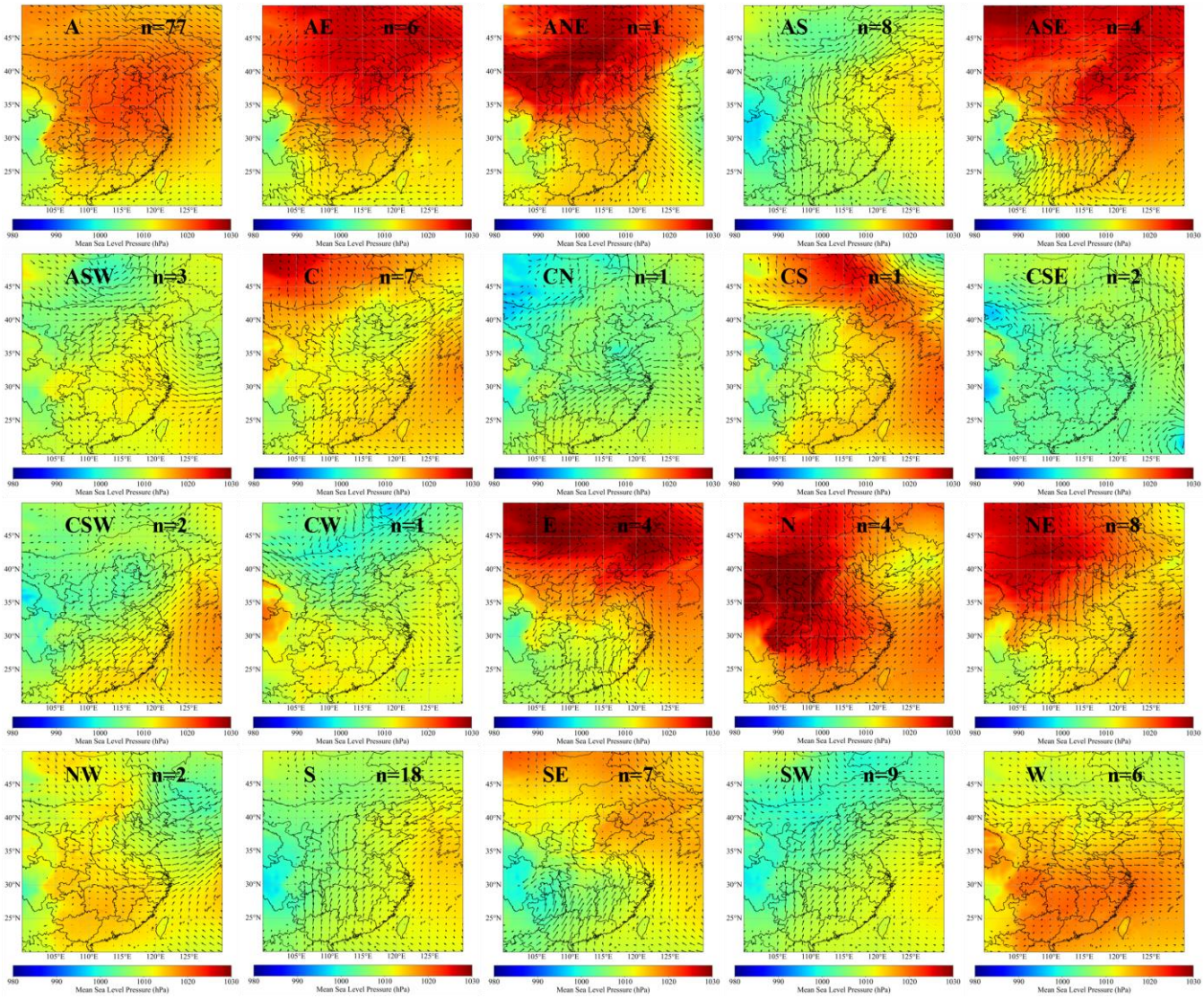

Figure S5: Spatial distribution of composite mean SLP and 850 hPa wind fields under different weather types (Preliminarily identified based on the Lamb-Jenkinson synoptic circulation classification method; n denotes the number of days).

5. Line 119: Please cite the HYSPLIT model formally (e.g., Stein et al., 2015).

Response 5: Thanks for reviewer's comments. We have now added the formal citation for the HYSPLIT model (Stein et al., 2015) to both the main text and the reference list.

Lines 164-165:

The hybrid single particle lagrangian integrated trajectory (HYSPLIT) is a common model for investigating meteorological transmission channels (Chen et al., 2024; Cheng et al., 2024; Shi et al., 2024; Stein et al., 2015).

6. Lines 131–136: Figure 1 indicates a secondary peak in June that is currently unaddressed. This feature should be interpreted in the context of seasonal ozone precursors or meteorological shifts.

Response 6: Thanks for reviewer's comments. The secondary peak in June is a crucial feature that requires explicit interpretation through the lens of seasonal precursor dynamics and meteorological shifts.

We have expanded our discussion to explicitly address this phenomenon. We now explain that the June peak is fundamentally driven by the coupling of these two factors:

(1) Meteorological shifts: June marks the onset of summer in the NCP, characterized by soaring temperatures and intensified solar radiation.

(2) Seasonal precursors: These warmer meteorological conditions directly trigger enhanced emissions of seasonal O_3 precursors (particularly biogenic VOCs).

The combination of abundant precursors and favorable photochemistry drives massive daytime O_3 accumulation. This generates a highly concentrated O_3 residual layer by dusk, which provides an abundant aloft reservoir that facilitates the occurrence of NOI events during this month.

Lines 183-193:

Additionally, all stations showed similar monthly variation trends: NOI days progressively increased from January to March, peaking in March (42-47 days), and then maintained high-level fluctuations from April to September. Notably, a distinct secondary peak is observed in June (Fig. 1). This early summer peak can be primarily attributed to the coupled effects of seasonal meteorological shifts and O_3 precursor dynamics. Meteorologically, June marks the transition to

summer in the NCP, characterized by sharp increases in temperature and intensified solar radiation. Concurrently, these warmer conditions significantly stimulate the enhanced emissions of natural ozone precursors (e.g., biogenic VOCs). The combination of abundant precursors and highly favorable meteorological conditions drives intense daytime photochemical O_3 production. This vigorous daytime accumulation generates a highly concentrated O_3 residual layer by dusk, which ultimately acts as an abundant aloft source for NOI events. Subsequently, the frequency reaches another peak in September (32-44 days) before declining sharply from October to December, reaching annual minima (15-26 days). This indicated that warm seasons favor NOI occurrence.

7. Section 3.4.1: When identifying geographical source areas via back-trajectories, the authors should discuss the known precursor emission profiles of those regions to provide a more robust chemical context.

Response 7: Thanks for reviewer's comments. In the revised Section 3.4.1, we have added the necessary chemical context to the key source regions identified by the back-trajectories:

(1) For A-type: We highlighted that northern Henan and western Shandong are regions well-documented for their heavy industrial facilities and intense precursor emissions.

(2) For S-type: We specified that the Central China urban agglomeration is characterized by intense anthropogenic NO_x and VOCs emissions, which act as the fundamental fuel for the massive O_3 accumulation observed in our CWT results.

By briefly contextualizing these emission profiles, the manuscript now provides a more robust bridge between the regional photochemical generation (daytime) and the subsequent advective/vertical transport (nighttime).

Lines 376-381:

Under A-type, air masses predominantly originated from the north (58.69%) (Fig. 8(a)). Crucially, the 3D altitude profiles (Fig. S8(a)-(b)) reveal that these dominant clusters originated from significantly high altitudes (~800 hPa) 48 hours prior, exhibiting continuous and massive subsidence as they approached Xinxiang. When these subsiding trajectories passed over the high O_3 potential source areas in northern Henan and western Shandong (CWT: 90-100 μg m^{-3}; Fig. 9(a)), regions well-documented for their heavy industrial facilities and intense precursor emissions (Lu et al., 2019; Li et al., 2019), they effectively entrained O_3-rich air from the residual layer downwards.

Lines 387-391:

Influenced by strong geostrophic winds under S-type, southwest airflow pathways dominated (Fig. 8(c)). The CWT analysis (Fig. 9(c)) identified a vast high-value source region (WCWT > 100 μg m^{-3}) encompassing the Central China urban agglomeration to the south, a vast region where intense anthropogenic NO_x and VOCs emissions continuously fuel massive daytime photochemical O_3 accumulation. The vertical profiles (Fig. S8(e)-(f)) confirm that a major portion of this southerly advection (~45.29%) subsided from the upper boundary layer (~880 hPa).